Available online at www.sciencedirect.com
ScienceDirect
Nuclear Instruments and Methods in Physics Research A 587 (2008) 35–45
NUCLEAR INSTRUMENTS & METHODS IN PHYSICS RESEARCH Section A
www.elsevier.com/locate/nima

Design of the recoil mass separator St. George

M. Couder[a], G.P.A. Berg[a,*], J. Görres[a], P.J. LeBlanc[a], L.O. Lamm[a], E. Stech[a], M. Wiescher[a], J. Hinnefeld[b]

[a]*Department of Physics, The Joint Institute for Nuclear Astrophysics, University of Notre Dame, Notre Dame, IN 46556, USA*
[b]*Department of Physics, Indiana University South Bend, South Bend, IN 46634, USA*

Received 1 August 2007; received in revised form 15 November 2007; accepted 21 November 2007
Available online 14 December 2007

Abstract

A recoil mass separator has been designed for the purpose of studying low energy (α,γ) reactions in inverse kinematics for beam masses up to about $A = 40$. Their reaction rates are of importance for our understanding of energy production and nucleosynthesis during stellar and explosive helium burning. The reactions take place in a windowless He gas target at the beginning of the separator which consists of three sections. The first section selects the most abundant charge state. The Wien filter in the second section efficiently separates the intense beam from the few reaction products. In the last section the reaction products are focused into a detector system consisting of time pickup and energy detectors. In order to accept the complete kinematic cone of recoil particles for energies as low as reasonably possible we specified a large circular angular acceptance of ±40 mrad. This requires a careful minimization of higher-order aberrations. The present system has been designed to allow for a future upgrade to extend the experimental program to the analysis of (p,γ) reactions.

PACS: 07.55.−w; 07.55.+h; 29.30.Aj; 41.85.−p; 41.75.−i; 25.40.Lw; 26.50.+x

Keywords: Recoil mass separator; Wien filter; Radiative alpha capture

1. Introduction

The radiative captures of protons and alpha particles represent the two important reaction mechanisms which characterize stellar hydrogen and stellar helium burning. Capture reactions dominate typical hydrogen burning sequences such as the pp-chains in low mass stars as well as the CNO, NeNa, and MgAl cycles in core and shell hydrogen burning in massive stars. Alpha capture reactions dominate critical reaction sequences in stellar helium burning which affect subsequent stellar evolution and the production of heavy nuclei through s-process nucleosynthesis. The experimental study of these reactions [1] has traditionally been conducted using intense, low energy proton and alpha beams. The nuclear reaction cross-sections were measured by detecting the characteristic γ rays emitted from the reaction products. The cross-sections drop exponentially toward stellar energies and the measurements of the associated γ radiation are handicapped by background radiation which severely limits the possibility of direct measurement of stellar reaction cross-sections. Consequently, the presently available stellar reaction rates are mostly based on often unreliable extrapolation of higher energy data to the stellar energy range [2].

The three main background components are cosmic ray induced radiation, natural radiation in the surrounding environment and beam induced background radiation from low Z target impurities. Underground experiments have been performed at the LUNA facility in the Gran Sasso Laboratory to reduce the cosmic ray induced background [3]. While these experiments have been successful, the natural background from the surrounding rock strata remains a limiting factor, especially for experiments on low Q-value capture reactions [4,5]. Several proposals of underground experiments in salt layers are presently being

*Corresponding author. Tel.: +1 574 631 6238; fax: +1 574 631 5952.
E-mail address: gpberg@bergs.com (G.P.A. Berg).

0168-9002/$ - see front matter © 2007 Elsevier B.V. All rights reserved.
doi:10.1016/j.nima.2007.11.069

discussed to reduce the natural background component. While this approach may provide a cleaner environment, it does not remove beam induced background from low Z impurities in the target material. For this reason alternative approaches have been suggested. Of particular interest is the inverse kinematics technique with high intensity heavy ion beams on hydrogen or helium gas targets. This technique allows the measurement of not only the reaction induced γ radiation but also of the reaction products with a recoil separator system installed in the forward direction. In a pioneering experiment Kremer et al. [6] employed the technique of inverse kinematics to the astrophysical reaction $^{12}C(\alpha,\gamma)^{16}O$ and showed that coincidences between γ radiation and recoil particles provide a very efficient tool for reducing all three background components.

In order to study reactions of explosive hydrogen burning in the hot CNO cycles and the rp-process [7] inverse kinematic experiments for low energy nuclear astrophysics experiments with radioactive beams were subsequently employed at several facilities. The DRS separator at the HRIB facility in Oak Ridge [8], the DRAGON separator at TRIUMF [9] and the ARES separator at Louvain-la-Neuve [10] have been the pioneering instruments for the first successful inverse kinematic experiments with low energy radioactive beams. In addition to the recoil mass separators (RMS) at radioactive beam facilities, the ERNA separator [11] at the DTL laboratory in Bochum has been installed to measure low energy reactions with stable beams in inverse kinematics. Very high beam suppression was demonstrated for these systems allowing measurements at energies lower than is possible with the traditional γ detection method.

The existing recoil separators are primarily designed for specific reactions. DRAGON was developed for the measurement of the $^{15}O(\alpha,\gamma)^{19}Ne$ reaction which served as benchmark for the design. ERNA was built with the goal of measuring $^{12}C(\alpha,\gamma)^{16}O$ in inverse kinematics. These facilities have provided very important information on the use and challenges of recoil separators for low energy experiments and have also shown that further development is necessary to exploit the full potential of this technique. In inverse kinematics, the beam and the reaction products are contained in a narrow cone at forward angles. A rejection of the beam is required to be able to detect the rare reaction products. The momentum of the beam and reaction products is nearly identical so that magnetic analysis alone does not provide sufficient separation. Therefore, the system must exploit the difference Δm in the masses of the beam and the reaction product, i.e. $\Delta m = 4$ for (α,γ). This can be accomplished by using a Wien filter with crossed magnetic and electric fields. Particles with velocity $v = E/B$ travel unaffected through a Wien filter while particles with different velocities are deflected, hence the name "velocity filter". In our case where the momentum $p = m \cdot v$ is fixed for a given beam energy, the Wien filter acts as a "mass filter".

Demanding challenges are associated with the need for high beam intensity and rejection ratio, the relatively large momentum transfer in low energy capture reactions and the wide charge state distribution of the emerging reaction products, all of which limit the efficiency of the recoil detection device. Because of the very small reaction rates of capture reactions at low energy, high beam intensities are required. This in turn necessitates a high beam to product separation ratio. The very low energy of the beam particles and reaction products prohibits the relatively simple and effective "wedge method" [12,13] which is often utilized for mass separation at higher energies. With decreasing energies and masses the angular cone in inverse kinematics becomes larger and the acceptance angle of the system has to be increased accordingly to efficiently collect the rare reaction products. This makes the magnets rather large and higher-order aberrations must be corrected, adding to the complexity and cost of such a system. While the detector system is able to identify particles that arrive at the end of the system, it is paramount to physically reduce the background as much as possible. Such background results from interactions of the intense beam with the residual gas, apertures, slits and walls of the vacuum chambers.

All these somewhat conflicting conditions must be considered and incorporated in an optimized recoil separator suitable for the intended astrophysical studies. On the basis of known principles and being guided by other recoil separators, we have designed a system, St. George, that is optimized for the low energy (α,γ) reactions in inverse kinematics for beam masses up to about $A = 40$. St. George is the acronym for Strong Gradient Electromagnetic Online Recoil separator for capture Gamma Ray Experiments. In the following section we will describe the design concept and general layout of the recoil separator. Then, we will discuss the ion optics, the design of the magnets and Wien filter and conclude the article with a summary.

2. Design of the recoil separator

To begin the design of the magnetic separator we identified a number of (α,γ) and (p,γ) reactions of astrophysical interest to be able to define the required design parameters suitable for these reactions. Table 1 shows sample (α,γ) reactions and several parameters relevant for the design. The estimated minimum energy shown in column 3 is determined by the smallest expected reaction yield that translates into four reactions per hour for a beam current of 100 μA resulting approximately in a measured rate of one event per hour. The maximum energy limit is given by the terminal voltage of 4 MV of the existing KN accelerator in the Nuclear Science Laboratory of the University of Notre Dame and the charge states expected from the ion source. As can be seen from column 8 an angular acceptance of about ±40 mrad is needed to transmit all sample reactions.

Table 1

Inverse (α,γ) reactions of astrophysical interest

Beam	Recoil	Beam E_{lab} (MeV)	E_{cm} (MeV)	Recoil E_{lab} (MeV)	Recoil Q [14]	Recoil abund. (%)	Half angle (mrad)	E range ±%	Mom. p (MeV/c)	$B\rho$ (T m)
^{16}O	^{20}Ne	5.8	1.16	4.64	5	42	14.2	2.8	415.7	0.277
		12.5	2.5	10.02	6	40	11.8	2.4	610.9	0.340
^{18}O	^{22}Ne	1.94	0.35	1.59	3	38	39.2	7.8	177.1	0.284
		3.3	0.60	2.70	4	42	30.9	6.2	332.6	0.277
^{34}S	^{38}Ar	10.0	1.05	8.95	8	32	10.4	2.1	795.7	0.332
		38.0	4.00	34.00	12	32	7.2	1.4	1551.0	0.431
^{36}Ar	^{40}Ca	12.5	1.25	11.25	9	31	9.1	1.8	915.3	0.339
		40.0	4.00	36.00	13	30	6.7	1.3	1638.0	0.420

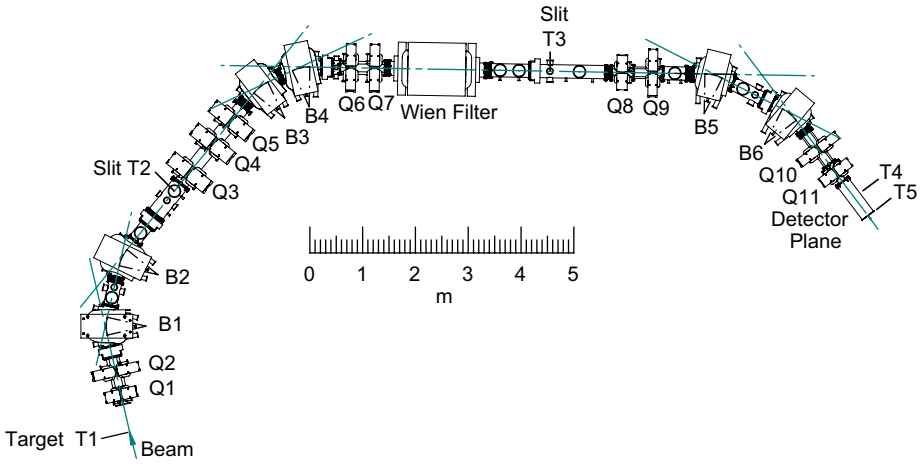

Fig. 1. Layout of the St. George recoil separator.

Another crucial design parameter is a large mass separation. Since the beam intensity is typically more than 15 orders of magnitude larger than the reaction products, the separation between the beam and reaction products has to be of the order of 10σ, assuming a Gaussian peak with a standard deviation of σ for the beam and reaction products at the selection position. This translates into a mass separation of approximately $m/\Delta m = 100$ for the (α,γ) reaction and a factor of at least four better for the (p,γ) reaction.

The following list of criteria was established to develop a concept for the separator and to specify the design parameters:

(1) Efficient measurement of the (α,γ) reaction in inverse kinematics in the beam mass range of up to $A = 40$, see sample reactions in Table 1.
(2) Separation of a single charge state by magnetic analysis after the target.
(3) Capability of handling high beam intensities.
(4) Effective separation of reaction products and beam with nearly identical magnetic rigidity, with a suppression factor $\geqslant 10^{15}$ and an effective mass separation of about $m/\Delta m = 100$, using a Wien filter.
(5) Ion optics for a helium jet gas target of 3 mm diameter.
(6) Ion optics including higher-order corrections that allows reaction products to be focused into a detector system with a diameter of 50 mm.
(7) A vacuum of 10^{-7} mbar is required in the separator.
(8) Optimal use of physical layout of the Nuclear Science Laboratory.

Based on these considerations a recoil separator with the layout shown in Fig. 1 was designed. While it is based upon concepts found in previous magnetic separators [9–11], the combination of ion optics with a specially designed Wien filter and the relatively large acceptance makes this instrument unique. A detailed description follows in the next section and the main design parameters are summarized in Table 2.

3. General layout

The complete system consists of a total of six dipole magnets (B1–B6), 11 quadrupole magnets (Q1–Q11) and one Wien filter. In addition to the vacuum chambers inside the magnetic elements, the beam line components provide space for vacuum pumps, valves, slits and other diagnostic

Table 2
Design parameters of the St. George magnetic recoil separator

Maximum rigidity $B\rho$	0.45 T m
Minimum rigidity $B\rho$	0.1 T m
Angle acceptance, vert., horiz.	±40 mrad
Energy acceptance	±7.5%
Mass separation $m/\Delta m$	≈ 100
Bending radius	75 cm

elements. All dipole magnet chambers have horizontal access ports for slits and zero degree ports for alignment and viewing at the entrances and exits. The abundance of ports provides the flexibility to insert beam stops and slits at a variety of locations to eliminate difficult to predict background for the variety of experiments that may be pursued. The separator is designed for use with a jet gas target with a diameter of 3 mm which will be installed at the target location T1. The thickness of the gas jet is typically 3×10^{17} atoms/cm^2 creating an energy loss of the beam of about 5 keV.

The complete separator consists of three *Sections* (S1, S2, and S3) organized according to their ion-optical functions.

- *Section* S1 extends from the target T1 to T2 and selects a specific charge state of both the beam and the reaction products. Beam and reaction products with different charge states will be eliminated with water cooled Faraday cups in appropriate locations near dipole B2.
- *Section* S2 extends from T2 to the slits T3 downstream of the Wien filter and provides the mass separation by means of the Wien filter. This *Section* is the most critical part of the system and separates the beam and reaction products of the selected charge state owing to the difference in mass with a very high beam suppression of $\geqslant 10^{15}$.
- *Section* S3 matches the phase space of the recoils to the requirements of the detector system and bends the particles through 52° via dipoles B5 and B6, providing additional background reduction. The vacuum chamber at the end of the separator, downstream of quadrupole Q11, serves as the detector chamber.

4. Ion optics

Extensive first-order ion-optical studies were conducted to design a recoil separator system that would satisfy the design criteria listed above. While the system is mainly designed to accommodate the desired reaction products, the ion optics of the separated beam must be considered for a variety of circumstances to stop the high intensity beam and to achieve a suppression of the order of $\geqslant 10^{15}$. Constraints of the existing building and beam lines for ongoing experiments required that the separator be very compact while maintaining the flexibility necessary for accommodating the range of the planned reaction studies. Special effort was made to minimize the number and the focusing strengths of the quadrupoles. This was achieved by adjusting the edge angles of the dipole magnets. It was, however, not possible to eliminate any of the present 11 quadrupoles without compromising one or more of the design requirements of the facility.

First-order design calculations of the beam and initial calculations of the separator were performed using the TRANSPORT code [15]. However, this code is ill suited for the optimization of the mass separation of the Wien filter and for calculations of higher orders. Therefore, all subsequent calculations were conducted using the COSY Infinity code [16]. Throughout this article we will use the notations as defined in COSY. Aberrations up to fourth order were calculated but only those up to third order were found to significantly affect the design parameters. These aberrations were reduced at T3 by shaping the boundaries of the 12 available dipole faces.

Results of the final ion-optical design calculations up to fourth order in both the horizontal x and vertical y directions along the central ray (z) are shown in Fig. 2. The calculations were performed for the maximum design rigidity of 0.45 T m with beam and recoil masses of $A = 36$ and 40, respectively. Both beam and recoil ions have the same charge of $Q = 11$. The acceptance parameters used in the calculations are summarized in Table 2. They include the most demanding cases that are extracted from Table 1. The complete system is 20.29 m long from the target location T1 to the detector plane T5. The upper panel shows the optics in the horizontal (x) plane. The effective field lengths (EFL) and good-field regions of the six dipole magnets B1–B6 are indicated by rectangles. For the quadrupoles Q1–Q11 the rectangles indicate the EFL in the z direction, while the transverse boundaries are given by two or three lines. When three lines are shown, they indicate the dimensions, starting from the inside, of the aperture radius, the good-field region and the physical limits of the vacuum chambers, respectively. The aperture radius is the radius of the largest clear circle between the pole pieces of a quadrupole magnet of the design shown in Fig. 5 with a diameter of 180 mm. When only two lines are shown the inner line represents the aperture radius and the outer line shows the vacuum chamber size. All quadrupole magnets are designed so that the good-field regions are at least as large as the aperture radii.

The lower panel shows the ion optics in the vertical direction. The EFL of the dipoles and quadrupoles are represented by the horizontal width of the rectangles. The vertical dimensions represent the gap for the dipoles and the inner dimensions for the vacuum chambers for the quadrupoles. The good-field regions are in all cases larger than the vacuum chambers.

To elucidate the ion optics, 11 horizontal and 7 vertical rays characteristic for the recoil separator are shown in Fig. 2. The starting values of the rays are listed in Table 3. The horizontal rays 1, 2, 3, 9, and 11 show the extreme rays

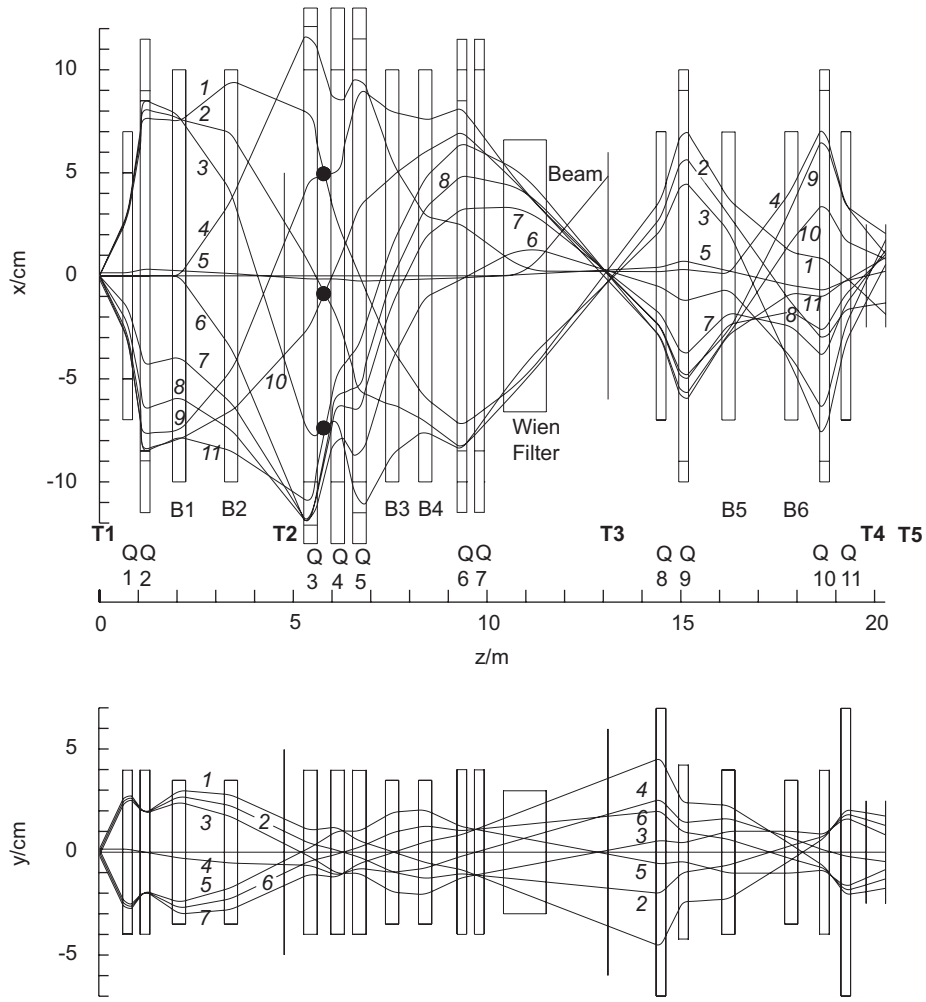

Fig. 2. Ion optics of the St. George recoil separator. The starting values of the rays are listed in Table 3. For details see text.

Table 3
Starting values of the 11 horizontal and 7 vertical rays shown in Fig. 2

Ray number	Horizontal rays			Vertical rays	
	x (mm)	Θ (mrad)	$\delta E/E$ (%)	y (mm)	Φ (mrad)
1	0	40	7.5	−1.5	40
2	0	40	0	0	40
3	0	40	−7.5	1.5	40
4	0	0	13	1.5	0
5	1.5	0	0	1.5	−40
6	0	0	−10.5	0	−40
7	0	−20	−9.5	−1.5	−40
8	0	−30	−9.0		
9	0	−40	7.5		
10	1.5	−40	0		
11	0	−40	−7.5		
Beam	0	0	0		

for the design acceptances of ±40 mrad for the angle and ±7.5% for the energy. The rays 5 and 10 explore the effects of a target size with a starting parameter 1.5 mm. Ray 5 shows the magnification along the system. The rays 4, 6, 7, and 8 test the energy acceptance as a function of angle. At 0° particles with an energy spread of ±10.5% will be transmitted, limited by the good-field region of quadrupole Q3. The accepted energy range will gradually decline with increasing angle. At the maximum transmitted design angle of ±40 mrad the accepted energy range is ±7.5%. All horizontal rays arrive at the plane T3 within a few millimeters in the horizontal direction. This was achieved by third-order corrections built into the dipole entrance and exit edges. The vertical ion optics is designed to keep all rays within the vertical gaps of the dipoles.

The vertical envelope near T3 is relatively large due to the vertical magnification $(y|y)$ with a maximum of about 15 in Q8 as can be seen from vertical ray 4. For a monoenergetic, point-to-point imaging the vertical magnification at a location z is defined as the ratio $(y|y) = y(z)/y(z = 0)$. For this reason, the vertical opening of the chambers of Q8 and Q9, as well as the gap of B5 is relatively large.

Section S1 is designed to eliminate all but one charge state from the distribution that is created in the target.

At and in front of T2 the dispersion is large, as can be seen from horizontal rays 4 and 6. Particles with all but the desired charge state are bent beyond the acceptance of the system and will be stopped in a slit system. The exact location of the slit system will depend on the experiment. Since the magnetic rigidity $B\rho$ is inversely proportional to the charge state, a good separation is achieved even for the smallest relative charge state of about $\Delta q/q = \frac{1}{10}$. For lighter nuclei the relative charge state can be significantly larger, e.g. $\Delta q/q = \frac{1}{3}$. For these cases beam access ports for slits are provided at the exit of dipole B2 and between B1 and B2.

In principle the best location for a charge state separation would be the focal plane of the subsystem. This focal plane is located between Q3 and Q4 and is identified by the intersections (marked by full circles) of three pairs of rays (1,9), (3,11), and (2,10). Due to the large dispersion all undesirable charge states are already outside of the acceptance at that location. The small emittance of the beam allows the elimination of the beam with different charge states on slits in front of the focal plane.

Desirable alternative designs with smaller dispersion, such as a smaller bending angle of B1 and B2 or a longer system could not be accommodated in the existing available space. This is mentioned here as it should be considered in the design of future recoil separators, where the above constraints are absent, as for example for a recoil separator design for a radioactive beam facility [17].

Since, for a given charge state, the momenta p and therefore the magnetic rigidities $B\rho = p/q$ of the beam and reaction products of the radiative capture reactions are nearly identical, no separation of beam and reaction products takes place in *Section* S1.

The crucial separation of beam and reaction products is accomplished in *Section* S2 by means of a Wien filter. The masses of beam and reaction products differ by four mass units for (α,γ) reactions. Since the momenta are the same, the mass difference of the beam and reaction products translates into a velocity difference and therefore a separation occurs in the Wien filter in *Section* S2. Apart from the Wien filter this *Section* consists of five quadrupole (Q3–Q7) and two dipole (B3 and B4) magnets. This *Section* optimizes the separation of the beam and reaction products at T3. This is demonstrated by the waist shown at T3 for the sample rays in the fourth-order calculation in the upper panel of Fig. 2. For a central ray of a point-to-point imaging the energy dispersion $(x|\delta E/E)$ is defined as the ratio of $x(z)$ and $\delta E/E$. The energy dispersion is ≈ 0 at T3 as can be seen from rays 4 and 6 with energy starting values of $\delta E/E = 13.0\%$ and -10.5%, respectively. A separation of the beam as seen in Fig. 2 is due to the mass difference of $\Delta m/m = \frac{1}{10}$ for the case of a beam mass of $A = 40$, the largest mass considered. In all other cases with $A < 40$, the separation is larger. The separation of 4–5 cm, or about 10σ, is needed in view of the huge difference between beam intensity and the rare reaction events. For a more detailed discussion of a realistic reaction see Section 5.

Considerable effort was dedicated to optimize the Wien filter for best performance and to minimize its size. This was important in view of the required large acceptance and the high beam suppression. In addition to the ion-optical functions of the magnets of *Section* S2 that are mentioned above, they also serve to maximize the mass separation for a given size of the Wien filter, as discussed in more detail in Section 7.

While the reaction products and the beam are in principle separated at location T3, it would be unrealistic to install a detector system here to identify the desired reaction products because of the expected, huge background [9–11]. Therefore, the reaction products are further transported through *Section* S3, which consists of four quadrupole (Q8–Q11) and two dipole (B5 and B6) magnets, from T3 to T4. The horizontal and vertical waist between B5 and B6 provides an opportunity to install apertures designed to further reduce background.

A detector system will be installed in the 50 cm drift space between T4 and T5. This length is suitable for a possible time of flight system for the low energy ions of interest. The vertical lines shown at these locations in Fig. 2 are ± 2.5 cm long. It should be mentioned that the emittances for realistic cases typically have a smaller envelope than defined by the extreme rays shown in Fig. 2. As an example, ray 4 is outside of the design acceptance and is shown purely to demonstrate the ion-optical properties and possible paths for background particles.

5. Simulation of a sample reaction

In order to demonstrate the optics for a realistic case, we performed a COSY calculation for the ^{22}Ne$(\alpha,\gamma)^{26}$Mg reaction in inverse kinematics. The ^{22}Ne ion had an energy of 4.6 MeV corresponding to a center of mass energy of 0.707 MeV. For the ^{4}He target we assumed a thickness of 3×10^{17} atoms/cm^2, a beam spot of 3 mm diameter and a beam angle opening of ± 2 mrad. Energy loss and straggling and angular straggling of the beam in the target volume were calculated using the Monte Carlo simulation of SRIM [18].

The upper panel of Fig. 3 shows the resulting horizontal envelopes of the reaction products, the beam with the most abundant 5^+ charge state [14] and the beam with a charge state 6^+. The lower panel shows the vertical envelope of the reaction particles. For an explanation of the coordinate system and the dimensions of the electro-magnetic elements see Fig. 2 and the corresponding text.

The reaction products and the 5^+ beam have a narrow waist at location T3, where the beam will be stopped. The reaction products travel through the center of the magnet system to the detectors at T4 and T5. Due to the relatively large difference in magnetic rigidity the 6^+ fraction of the beam is already separated for the reaction products in front of the magnetic dipole B2 and will be stopped there. The envelopes include 10^4 rays within the beam spot for the

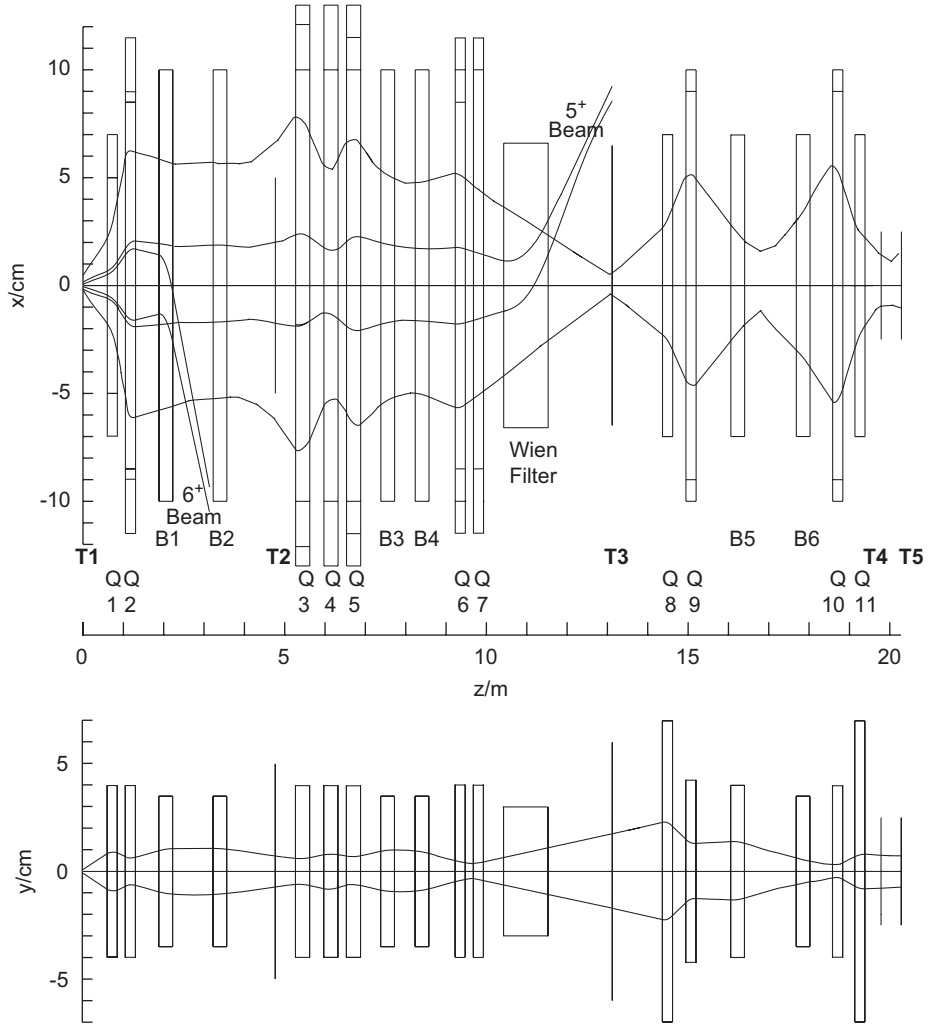

Fig. 3. Ion optics of the $^{22}Ne(\alpha,\gamma)^{26}Mg$ reaction in inverse kinematics at 4.6 MeV incident energy. Shown are the horizontal envelopes of the 5^+ reaction products, and the most abundant 5^+ and the 6^+ beams. The lower panel shows the vertical envelope of the reaction products.

reaction products and the beam was transported through the system by a fourth-order COSY calculation.

This calculation shows that all rays are well within the acceptance of the system. This ion-optical calculation does not include particles that may be scattered by the residual gas.

6. Magnet design

The magnets are designed to provide the good-field region required in both transverse directions and the necessary field strengths according to the ion-optical calculations. All magnets are operated by highly stabilized direct currents and are designed to operate at fields up to 0.6 T in the gap of the dipoles and 0.3 T at the pole tips of the quadrupoles so that iron saturation can be kept negligible. For this reason, all iron pole pieces and return yokes are machined of solid, soft magnet iron. All coils are normal conducting with hollow copper conductors to allow water cooling. The coil temperatures are kept below 55 °C. All magnets including vacuum chambers, power supplies, and supports are manufactured by the commercial vendor Bruker Biospin which has significant experience in the design and construction of similar magnet systems.

6.1. Dipole magnets

The six dipoles are H type magnets. They will be manufactured according to the specifications given below and in Table 4. All dipole magnets have a bending radius of 750 mm and bend particles through an angle of 26° as shown in Fig. 4 for dipole B1. The gaps of all dipoles are 70 mm except for B5 which has a gap of 80 mm. The horizontal good-field regions are 200 mm for B1–B4 and 140 mm for B5 and B6. This is accomplished with pole widths of 440 mm for B1–B4 and 380 mm for B5–B6 and with the help of Rose shims at the sides, not shown in this drawing. This ensures that the field is constant within $dB/B < 2 \times 10^{-4}$ in the good-field region. The maximum magnetic field B is 0.6 T to allow the bending of particles

Table 4
Design parameters of the dipole magnets

Parameter	Dipole magnet type					
	B1	B2	B3	B4	B5	B6
Good-field region, $dB/B < \pm 0.02\%$ (mm)	200	200	200	200	140	140
Entrance parameter a	0.23	0.13	0.23	0.23	0.23	0.10
Entrance parameter b (1/m)	−0.05	−0.74	−0.09	−0.67	0	0
Entrance parameter c (1/m^2)	2.8	0	0	0	0	0
Exit parameter a'	0.23	0.13	0.23	0.23	0.23	0.10
Entrance parameter b' (1/m)	0.25	−0.59	−0.61	0	0	0
Entrance parameter c' (1/m^2)	0	0	0	−0.32	0	0

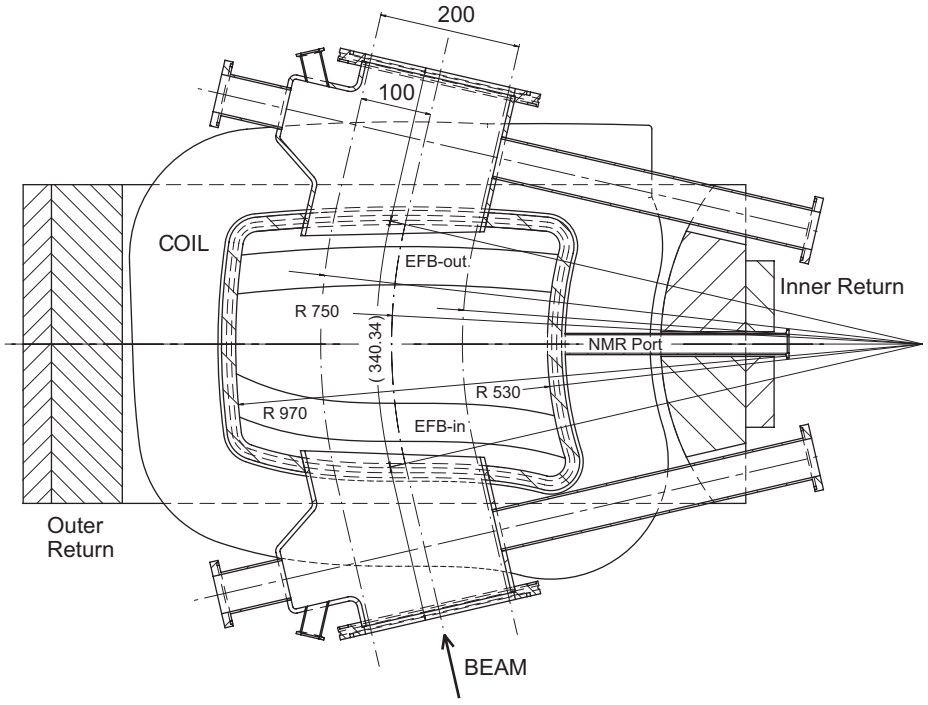

Fig. 4. View from above the midplane of dipole magnet B1 and the vacuum chamber. The physical shape of the pole piece at the entrance (EFB-in) and the exit (EFB-out) is designed to create the higher-order corrections. All dimensions are in millimeter.

with magnetic rigidities up to 0.45 T m. Each magnet weighs about 1000 kg and has a maximum power of 5 kW. The cross-sectional area of the inner and outer return yokes is approximately 40% of the pole surface, sufficient to keep the magnetic inductance below about 1.4 T in the outer yoke and 1.7 T in the inner yoke, where saturation effects begin to become noticeable.

The vacuum chamber of B1 shown in Fig. 4 has a number of access ports that are also available in the chambers of the other dipole magnets, whenever possible. Two large entrance and exit ports with 200 mm width and a height of 70 mm (80 mm for B5) ensure the clear passage of all particles within the acceptance. A port extended through the inner yoke allows the insertion of a NMR or Hall probe for precise field setting and monitoring. Two transverse ports at the entrance and exit of the magnet allow the installation of a variety of slits and diagnostic elements to stop and measure the beam or background, as may be required for a particular experiment. All vacuum chambers are of wrap-around type where the pole pieces serve as top and bottom lids. For cost reasons, easy access to the inside of the vacuum chambers, and to avoid magnetization during welding, seals are provided by Viton O-rings. All magnets have 0° ports in both directions for alignment and other access needs that may arise.

In order to meet the specifications, in particular the large design acceptances, higher-order corrections are necessary. Due to the limited space within the laboratory, it was not possible to include separate higher-order magnets in the system. However, higher-order corrections were provided by shaping the field boundaries at the entrances and exits of the dipole magnets. The optimum boundaries include up

Table 5
Quadrupole design parameters

Parameter	Quadrupole magnet type										
	Q1	Q2	Q3	Q4	Q5	Q6	Q7	Q8	Q9	Q10	Q11
Overall length (mm)	390	390	490	490	490	390	390	390	390	390	390
Focusing strength (T)	1.2	0.8	0.5	0.75	0.6	0.3	0.25	0.5	0.75	0.85	0.6
Eff. field length (mm)	250	250	350	350	350	250	250	250	250	250	250
Gradient (T/m)	4.80	3.20	1.43	2.14	1.71	1.20	1.00	2.00	3.00	3.40	2.40
Horiz. good-field region (mm)	94	180	242	170	230	185	160	120	185	185	110
Aperture diameter (mm)	100	170	200	200	200	170	170	140	180	180	140
Max. pole tip field (T)	0.22	0.25	0.13	0.19	0.15	0.09	0.09	0.13	0.24	0.28	0.15
Max. inhomogeneity (%)	0.2	0.2	0.2	0.2	0.2	0.2	0.2	0.2	0.2	0.2	0.2
Hor. pipe, inner diameter (mm)	140	230	260	260	260	230	230	140	200	200	140
Vert. pipe, inner diameter (mm)	80	80	80	80	80	80	80	140	85	80	140

to third-order terms. The boundaries are parameterized by polynomials as follows:

$$\text{Entrances: } z(x) = ax + bx^2 + cx^3$$
$$\text{Exits: } z(x) = a'x + b'x^2 + c'x^3.$$

Here $z(x)$ is the displacement in meter (positive is into the magnet) at the position x in meter, where x is the transverse coordinate with respect to the optical axis, with the origin where it crosses the field boundary. The coefficients of the optimized field boundaries are listed in Table 4. The first-order coefficients a and a' are the tangents of the edge rotation and provide vertical focusing. This focusing helps to minimize the vertical particle envelopes and therefore the gaps of the magnetic dipoles. It also reduces the maximum required focusing strengths of the quadrupole magnets.

The calculations for the higher-order corrections were performed with the following considerations in mind. We wanted a high mass resolution to achieve a good separation of beam and reaction products at T3. In addition the good-field regions of the magnets and the sizes at the detector locations T4 and T5 should be as small as possible. In most cases second-order hexapole corrections (b, b') were sufficient and only two boundaries required octupole corrections (c, c'). Calculations also showed that deviations of $0.002, 0.01\,\mathrm{m}^{-1}$, and $0.1\,\mathrm{m}^{-2}$ for the quadrupole, hexapole and octupole parameters, respectively, are acceptable and do not affect the performance of the system. Examples of the second- and third-order corrections at the exit and entrance of dipole magnet B1 can be seen in Fig. 4.

Despite extensive calculations it was not possible to further minimize the images at T3, T4, and T5 for the present configuration. This was considered acceptable since the required mass resolution at T3 was achieved and the sizes at T4 and T5 can be accommodated with achievable detectors.

Rather than attempting time consuming three-dimensional field calculations to predict the shape of the magnet ends for the proper edge angles and higher-order components, it was decided to build B1 as a prototype on the basis of two-dimensional calculations, map the field and make corrections as required. The expectation is that the dipole fields of the other magnets can then be produced without further shimming or field clamps.

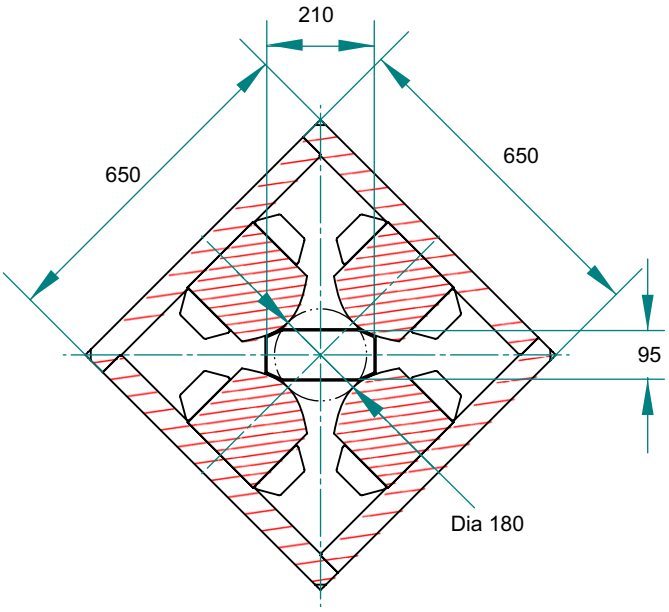

Fig. 5. Cross-section drawing of the quadrupole magnet Q10 including the vacuum chamber.

6.2. Quadrupole magnets

The 11 quadrupole magnets of the separator system will be manufactured according to the specifications in Table 5. Most quadrupole magnets require the dimensions of the horizontal good-field regions to be significantly wider than the vertical ones. In these cases the vacuum chambers are wider in the horizontal direction. As an example, the quadrupole Q10 is shown in Fig. 5. The inner diameter of this quadrupole is 180 mm. The required good-field region is vertically 80 mm and horizontally 185 mm, well within the inside clearances of the vacuum chamber. The pole

pieces will be shaped to provide a good-field region that is horizontally wider than the diameter between poles by up to 20% for most of the quadrupoles.

In order to be able to set the magnetic fields reproducibly, all dipoles have ports where NMR or precision Hall probes can be inserted as shown in Fig. 4. The hysteresis effects in the quadrupoles are small enough so that the quadrupole fields can be set by current.

7. Design of the Wien filter

The design of Wien filters poses several technical challenges, e.g. they can become large because the electro-static system must be installed inside the gap of the dipole magnet. With increasing size the electrode inside the magnetic dipole drives the height of the magnet quickly to impractical dimensions or results in a poor magnetic good-field region. Therefore, we have minimized the height of the electrodes with two pairs of homogenizing electrodes.

Fig. 6 shows a top view of the horizontal midplane of the Wien filter. The beam enters from the left and passes between the main electrodes. The lower pair of homogenizing electrodes is also shown. The main electrodes are mounted from the sides on ceramic supports and are connected in the center to the high voltage power supplies. The magnet coils, returns, and field clamps are shown surrounding the vacuum chamber. The EFL of both the magnetic and electric dipoles are 1100 mm. The good-field regions of both dipoles are 130 mm horizontally and 60 mm vertically with relative field homogeneities of ± 0.002. The vertical gap of the dipole magnet is 320 mm high to accommodate the electrodes mounted inside the vacuum chamber. The electrodes are 200 mm high and have a 48 mm spacing to the grounded upper and lower walls of the vacuum chamber. The horizontal gap is 132 mm wide and a maximum high voltage of ± 110 kV will be applied. The homogenizing electrodes are designed for a maximum voltage of ± 37 kV. A detailed discussion of the Wien filter will be presented in a forthcoming article [19].

Another challenge in designing Wien filters is the spatial difference in electric and magnetic fringe fields. Because of the large gap that has to include the electrode height and the safe distance to ground and properties inherent to magnetic dipoles, the magnetic fringe field extends over a larger distance than the electric fringe field. In this fringe field region, the ratio of E/B differs from that inside the Wien filter, and this can result in a significant degradation in the quality of the velocity filter. Several features have been incorporated into the design of the Wien filter in an effort to minimize the distortions in the fringe field region.

We first minimized the height of the electrodes, which reduces the magnet gap and therefore the length of the magnetic fringe field. In addition, the fringe field of the magnet was reduced as much as possible by the addition of adjustable field clamps. These field clamps provide the additional advantage that the EFB can be adjusted by approximately ± 10 mm to optimize the performance. This adds flexibility to the design in addition to reducing manufacturing costs by avoiding costly mapping/machining iterations if the calculated and measured EFB deviate.

The electrodes are designed so that the electric fringe fields are extended to closely follow the magnetic fringe field. This is accomplished by flaring open the electrode ends progressively as shown in Fig. 6 and by moving the grounded entrance and exit walls to a distance of about 218 mm from the ends of the electrodes. The resulting electrode design was optimized in two-dimensional calculations using the finite element field code MagNet [20] and then verified using the code SIMION [21] in three dimensions to ensure that the out of plane deviations do not affect the mass separation.

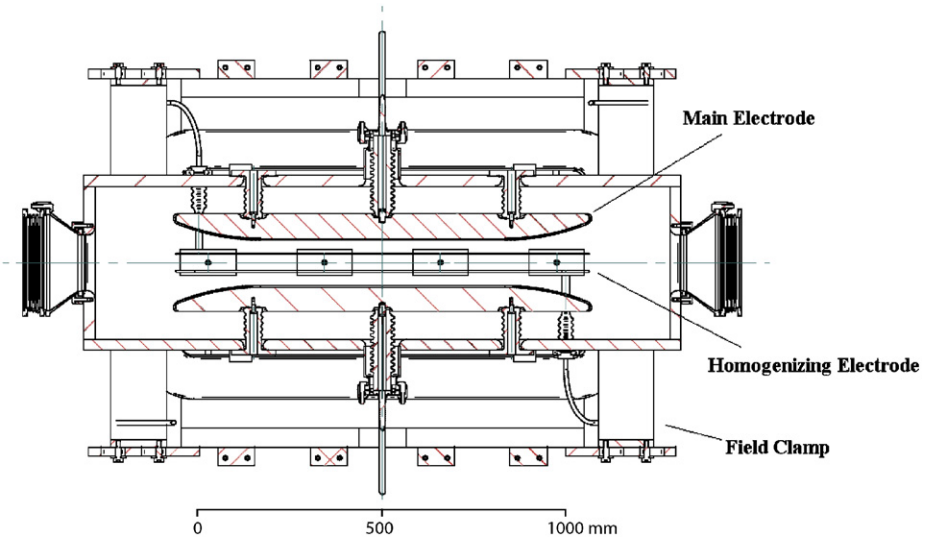

Fig. 6. A top view of the horizontal midplane of the Wien filter is shown. Electrostatic dipole is mounted inside the magnet.

The size of the Wien filter was minimized by a careful ion-optical design that maximizes the desired mass separation for a minimum good-field region.

8. Summary

A recoil separator has been designed with the goal to measure (α,γ) radiative capture reactions at very low energies in inverse kinematics that cannot be measured in present facilities or in direct kinematics. These measurements are very important to verify extrapolations of stellar reaction rates used in astrophysical studies. This requires large angular and energy acceptances of ± 40 mrad and $\pm 7.5\%$, respectively. Higher-order ion-optical correction is accomplished by shaping the entrance and exit field boundaries of the dipole magnets.

Inverse kinematics in combination with a recoil separator allows for the reduction of background further than possible in the direct reaction using an α beam. Separation of beam and reaction products is accomplished by first selecting a charge state and transmitting a fixed momentum. Then, a specially designed Wien filter is used for a mass selection of $m/\Delta m = 100$, resulting in a beam suppression of the order of $\geqslant 10^{15}$. Further background reduction is accomplished in a detector system at the end of the recoil separator.

The system is also designed to allow a later upgrade for (p,γ) experiments in inverse kinematics that require higher mass separations by about a factor of 4. This can be accomplished by modifying the last section of the present system and by adding additional Wien filters and/or electrical dipoles and magnet sections for background suppression and matching to the following detector system.

The recoil separator is presently under construction and commissioning is expected to begin in summer 2008 with experimentation to begin in fall 2008.

Acknowledgments

The authors would like to express their special thanks to Cary Davids and David Hutcheon for their helpful comments. This work is supported by the National Science Foundation under Grant No. PHY01-40324, the Joint Institute for Nuclear Astrophysics and the University of Notre Dame.

References

[1] C. Iliadis, A.E. Champagne, Nucl. Phys. A 758 (2005) 73c.
[2] A. Aprahamian, K. Langanke, M. Wiescher, Prog. Part. Nucl. Phys. 54 (2005) 535.
[3] R. Bonetti, et al., Phys. Rev. Lett. 82 (1999) 5205.
[4] D. Bemmerer, et al., Eur. Phys. J. A 24 (2005) 313.
[5] G. Imbriani, et al., Eur. Phys. J. A 25 (2005) 455.
[6] R.M. Kremer, C.A. Barnes, K.H. Chang, H.C. Evans, B.W. Filippone, K.H. Hahn, L.W. Mitchell, Phys. Rev. Lett. 60 (1988) 1475.
[7] H. Schatz, A. Aprahamian, J. Görres, M. Wiescher, F.K. Thielemann, T. Rauscher, J.F. Rembges, B. Pfeiffer, P. Möller, K.L. Kratz, H. Herndl, B.A. Brown, H. Rebel, Phys. Rep. 294 (1998) 167.
[8] R. Fitzgerald, et al., Nucl. Phys. A 748 (2005) 351.
[9] D.A. Hutcheon, et al., Nucl. Instr. and Meth. A 498 (2003) 190.
[10] M. Couder, C. Angulo, W. Galster, J.-S. Graulich, P. Leleux, P. Lipnik, G. Tabacaru, F. Vanderbist, Nucl. Instr. and Meth. A 506 (2003) 26.
[11] D. Rogalla, et al., Nucl. Instr. and Meth. A 513 (2003) 573.
[12] J.P. Dufour, R. Del Moral, H. Emmermann, F. Hubert, D. Jean, C. Poinot, M.S. Pravikoff, A. Fleury, Nucl. Instr. and Meth. A 248 (1986) 267.
[13] G.P.A. Berg, O.C. Dermois, U. Dammalapati, P. Dendooven, M.N. Harakeh, K. Jungmann, C.J.G. Onderwater, A. Rogachevskiy, M. Sohani, E. Traykov, L. Willmann, H.W. Wilschut, Nucl. Instr. and Meth. A 560 (2006) 169.
[14] R.O. Sayer, Rev. Phys. Appl. 12 (1977) 1543.
[15] PSI Graphic Transport Framework by U. Rohrer based on the CERN-SLAC-Fermilab version by K.L. Brown, D.C. Carey, C. Iselin, F. Rotacker, CERN 73-16, 1973 and CERN 80-04, 1980.
[16] M. Berz, COSY Infinity ⟨http://www.bt.pa.msu.edu/index_files/cosy.htm⟩.
[17] Isotope Science Facility at Michigan State University, MSUCL-1345, November 2006.
[18] J.F. Ziegler, J.P. Biersack, U. Littmark (Eds.), The Stopping and Ranges of Ions in Matter, vol. 1, Pergamon Press, New York, 1985. J.F. Ziegler, SRIM-2006, v. 2006.01 ⟨http://www.srim.org⟩.
[19] G.P.A. Berg, M. Couder, J. Görres, P.J. LeBlanc, L.O. Lamm, E. Stech, M. Wiescher, J. Hinnefeld, to be published.
[20] Finite Element Code MagNet, Infolytica Corporation, Montréal, Canada.
[21] D.A. Dahl, Int. J. Mass Spectrom. 200 (2000) 3.